

Characterization of woodstove briquettes from torrefied biomass and coal

Anna Trubetskaya^{a,b,*}, James J. Leahy^c, Elena Yazhenskikh^d, Peter Layden^e, Robert Johnson^e, Kenny Ståhl^f, Rory F.D. Monaghan^{a,b}

^a*Mechanical Engineering Department, National University of Ireland Galway, Galway, Ireland*

^b*Research Centre for Marine and Renewable Energy, Galway, Ireland*

^c*Department of Chemical Sciences, University of Limerick, Limerick, Ireland*

^d*Forschungszentrum Juelich GmbH, 52425 Juelich, Germany*

^e*Arigna Fuels, Arigna Carrick-on-Shannon Co. Roscommon, Ireland*

^f*Department of Chemistry, Technical University of Denmark, Kemitorvet B206, 2800 Kongens Lyngby, Denmark*

S-1. Sieving

A vibrating sieve shaker AS 200 (Retsch Technology, Germany) comprising nine sieves ranging from 0.075 to 4 mm in opening size and a bottom pan was used. The sieving analysis is described in EN ISO 17827-2:2016. Particles remaining on each sieve and in a bottom pan were collected and weighed using an electronic top pan balance (± 0.01 g accuracy). The cumulative retained undersize is the mass passed from the previous sieve minus the mass retained on the current sieve [1]. Sieving was conducted for 15 min at 3 mm amplitude [2].

S-2. Laser diffraction

Particle size distribution of original and torrefied samples was determined by a 3000 particle size analyzer (Malvern Instruments Ltd, UK) using a wet

*Corresponding author. anna.trubetskaya@nuigalway.ie

method. Biomass samples were dispersed in Ethanol. All measurements were made at room temperature and at 2400 rpm on at least two samples. Refractive indices of feedstock and ethanol were taken as 1.468 and 1.36, respectively [3]. The Sauter mean diameter was calculated as the surface area moment mean, and defined as

$$D_{32} = \frac{\sum n_i d_i^3}{\sum n_i d_i^2}. \quad (1)$$

The volume mean diameter (D_{43}) was calculated as follows

$$D_{43} = \frac{\sum n_i d_i^4}{\sum n_i d_i^3}, \quad (2)$$

where n_i is the number of particles with measured diameter d_i .

S-3. Ash compositional analysis

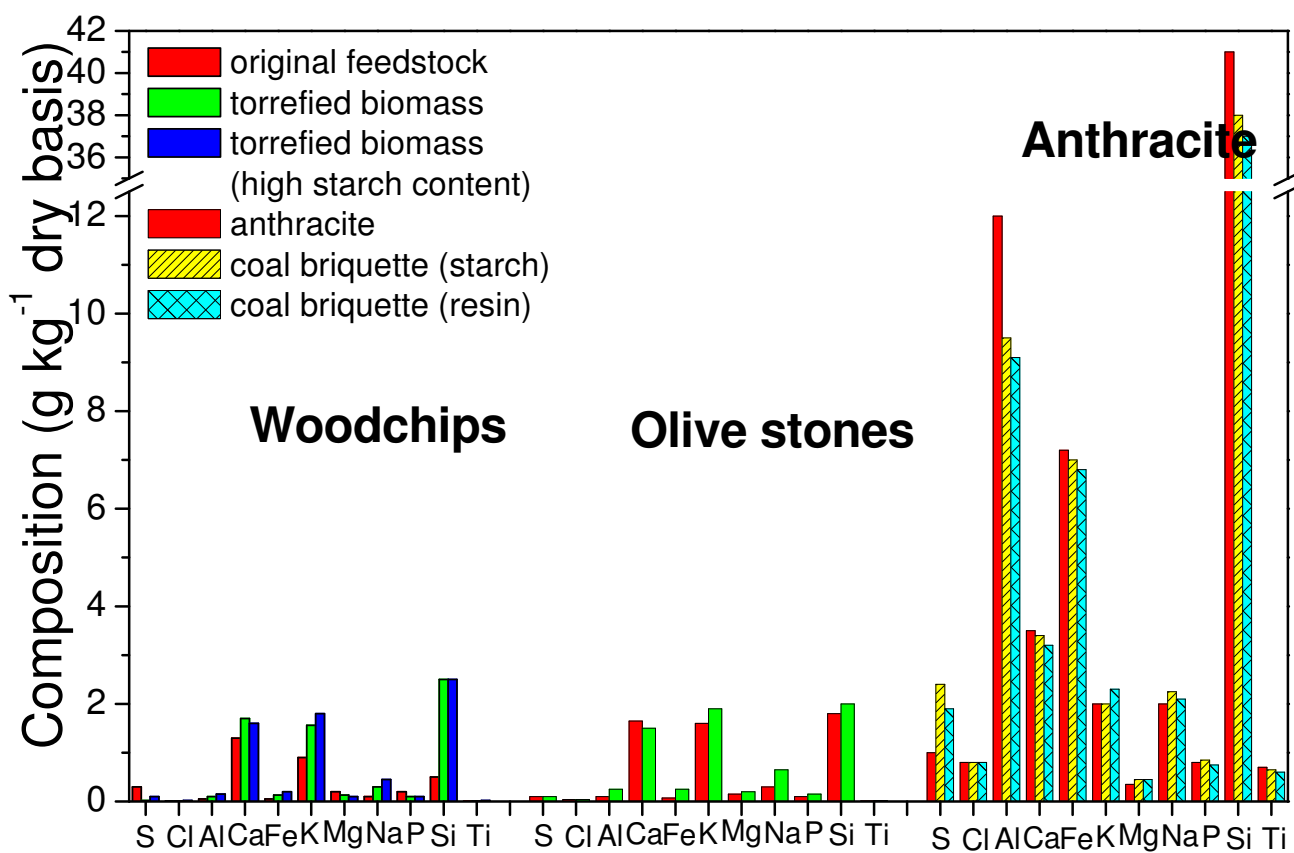
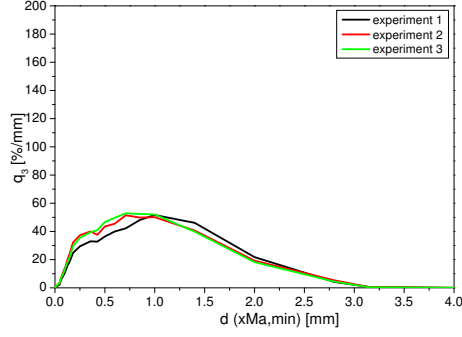
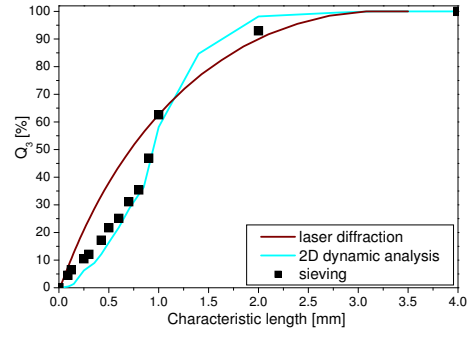


Figure S-1: Ash compositional analysis of olive stones and woodchips, torrefied material, torrefied woodchips with the high binder content, anthracite, and pulverized coal briquettes using a starch or resin as a binder which is shown in g kg^{-1} on the dry ash basis of original feedstock.

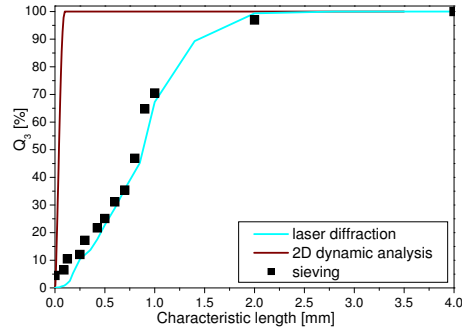
S-4. Particle size and shape



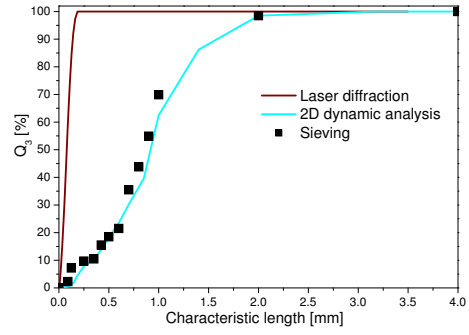
2(a): Repeatability of CAMSIZER measurements



2(b): Torrefied woodchips

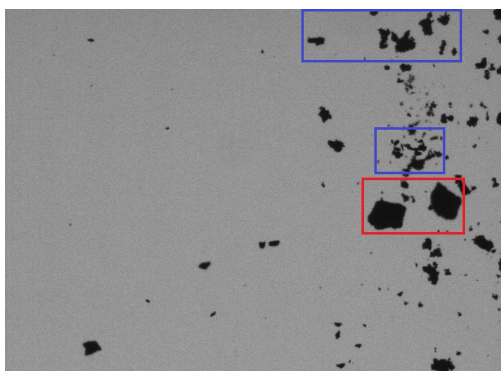


2(c): Torrefied olive stones

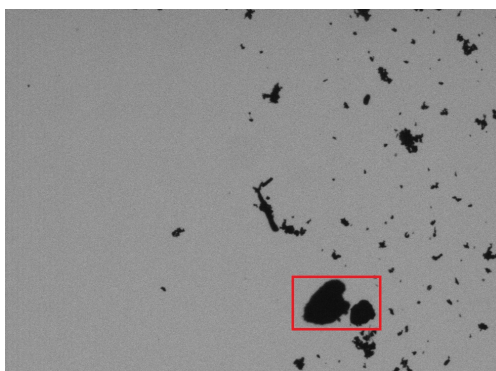


2(d): Coal briquette

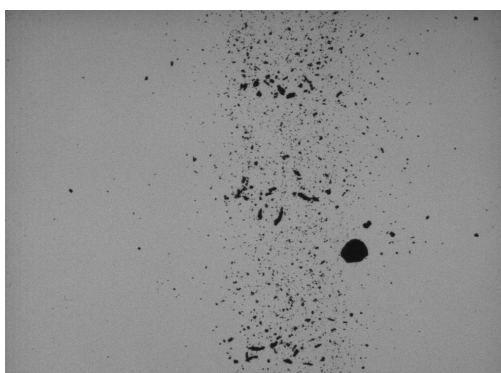
Figure S-2: (a) Repeatability measurements by 2D dynamic instrument using anthracite and (b-d) comparison of sieving, laser diffraction and 2D dynamic measurements using torrefied woodchips, torrefied olive stones, and pulverized coal briquette with the starch binder.



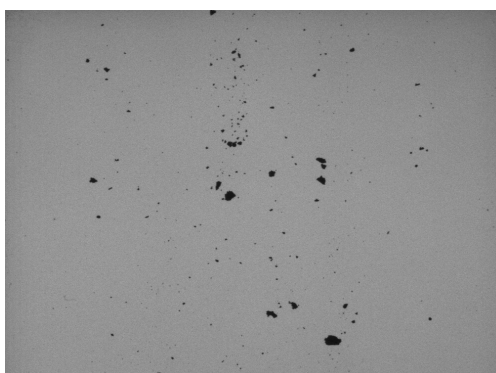
3(a): Anthracite



3(b): Pulverized coal briquette (starch)



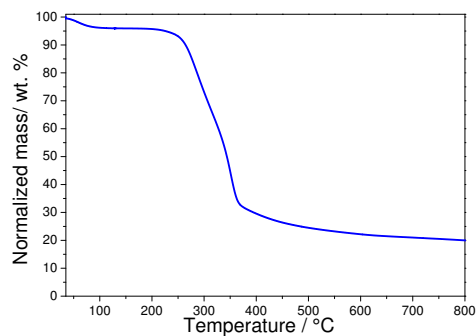
3(c): Olive stones



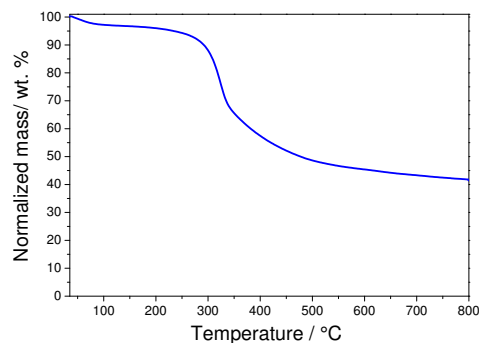
3(d): Torrefied olive stones

Figure S-3: 2D images of anthracite, pulverized coal briquette, olive stones and torrefied olive stones from CAMSIZER analysis.

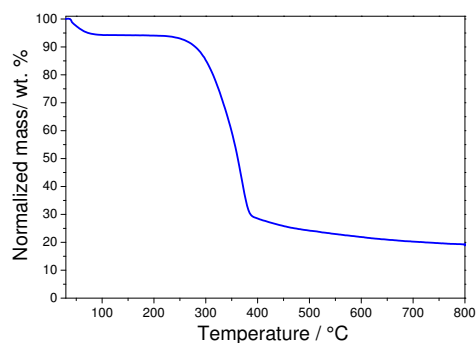
S-5. Thermogravimetric analysis



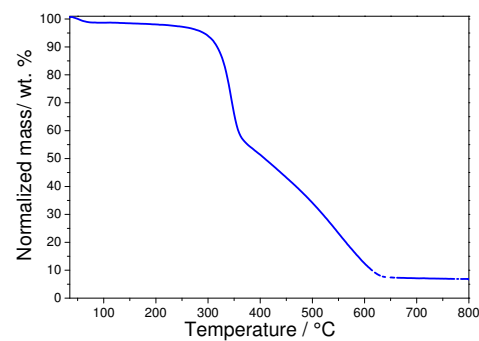
4(a): Olive stones



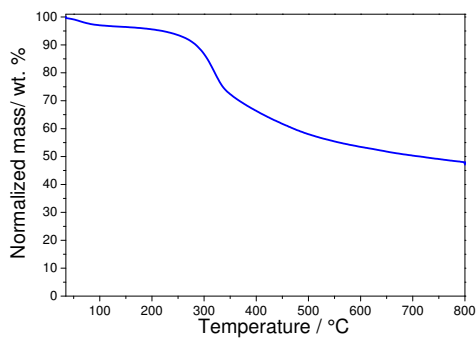
4(b): Torrefied olive stones



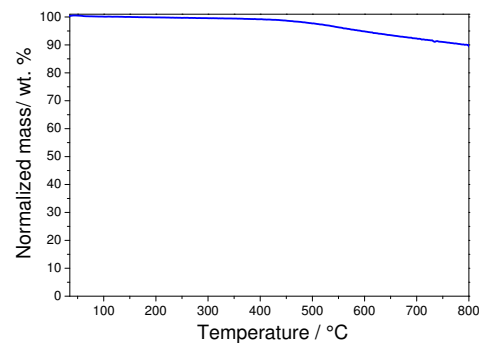
4(c): Woodchips



4(d): Torrefied woodchips

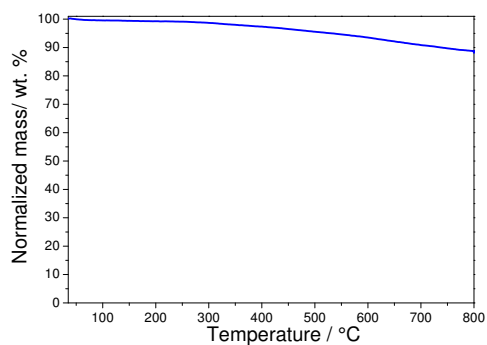


4(e): Torrefied woodchips (high binder)

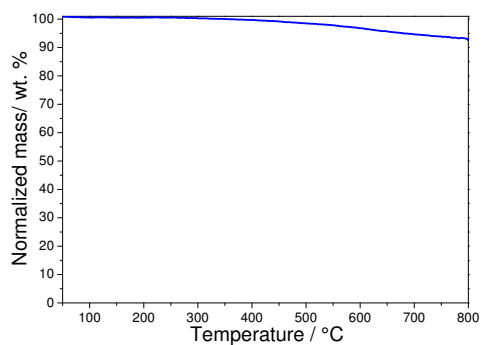


4(f): Olive stones

Figure S-4: Thermogravimetric analysis in 100 % volume fraction N_2 flow of olive stones and woodchips, torrefied material, torrefied woodchips with the high binder content, and anthracite.



5(a): Pulverized coal briquette (starch)



5(b): Pulverized coal briquette (resin)

Figure S-5: Thermogravimetric analysis in 100 % volume fraction N_2 flow of pulverized coal briquette using starch or resin as a binder.

Table S-1: Kinetic parameters for CO₂ reactivity of olive stones and woodchips, torrefied material, torrefied woodchips with the high starch content, anthracite, pulverized coal briquette using starch or resin as a binder reacted in 20 % volume fraction CO₂ + 80 % volume fraction N₂.

E_a	A	r_{max} at 700°C
kJ mol^{-1}	s^{-1}	s^{-1}
Olive stones		
187	$6.4 \cdot 10^5$	2.6
Torrefied olive stones		
198	$9.5 \cdot 10^9$	0.2
Woodchips		
142	$2.3 \cdot 10^7$	0.5
Torrefied woodchips		
129	$2.1 \cdot 10^6$	0.2
Torrefied woodchips with the high starch content		
99.2	$1.3 \cdot 10^4$	0.06
Anthracite		
103.4	$6.4 \cdot 10^5$	1.8
Pulverized coal briquette (starch)		
90.3	$3.9 \cdot 10^2$	0.01
Pulverized coal briquette (resin)		
97.6	$7.2 \cdot 10^2$	0.01

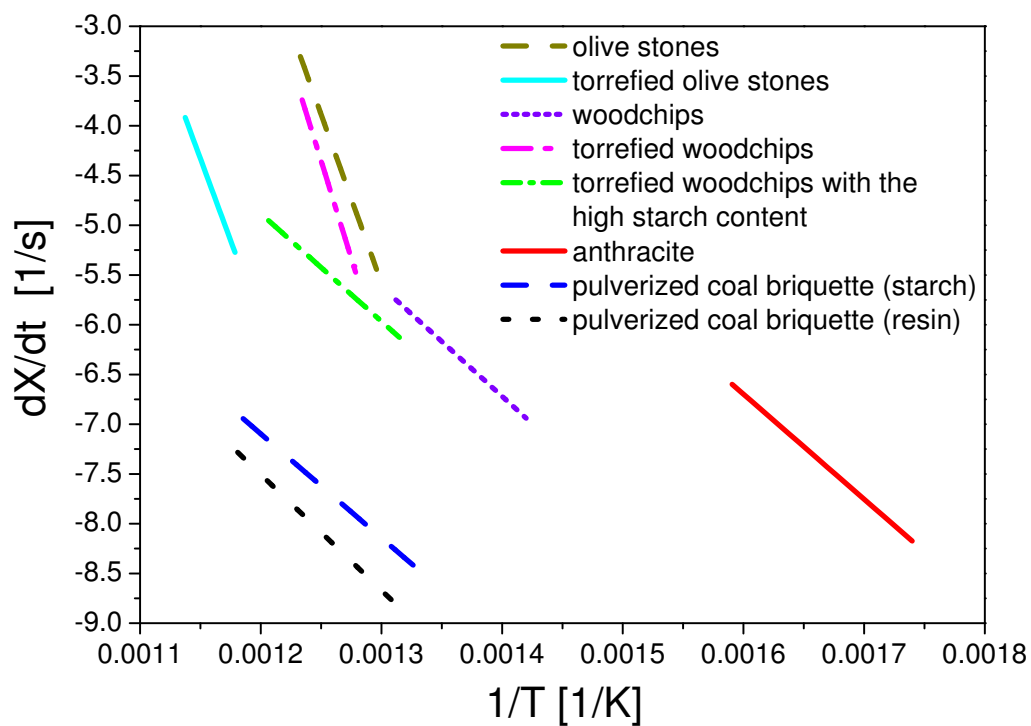
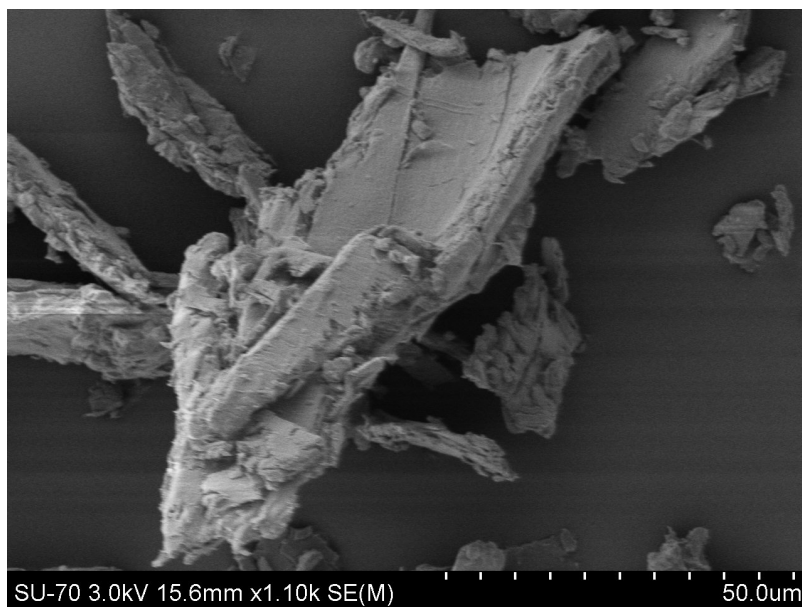
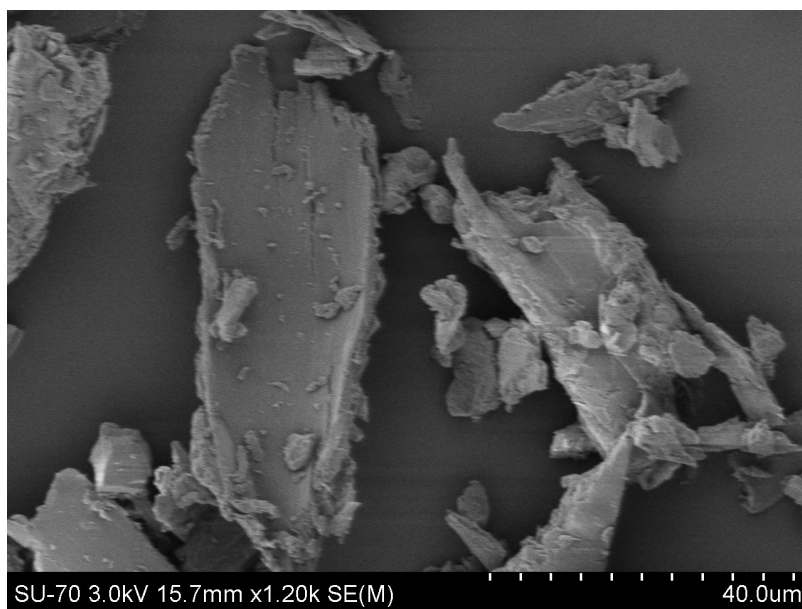


Figure S-6: Arrhenius plot of CO_2 reactivity of olive stones and woodchips, torrefied material, torrefied woodchips with the high starch content, anthracite, pulverized coal briquette using starch or resin as a binder reacted in 20 % volume fraction CO_2 + 100 % volume fraction N_2 .

S-6. SEM analysis



7(a): Torrefied woodchips



7(b): Torrefied woodchips

Figure S-7: SEM analysis of torrefied woodchips.

S-7. Pore size distributions

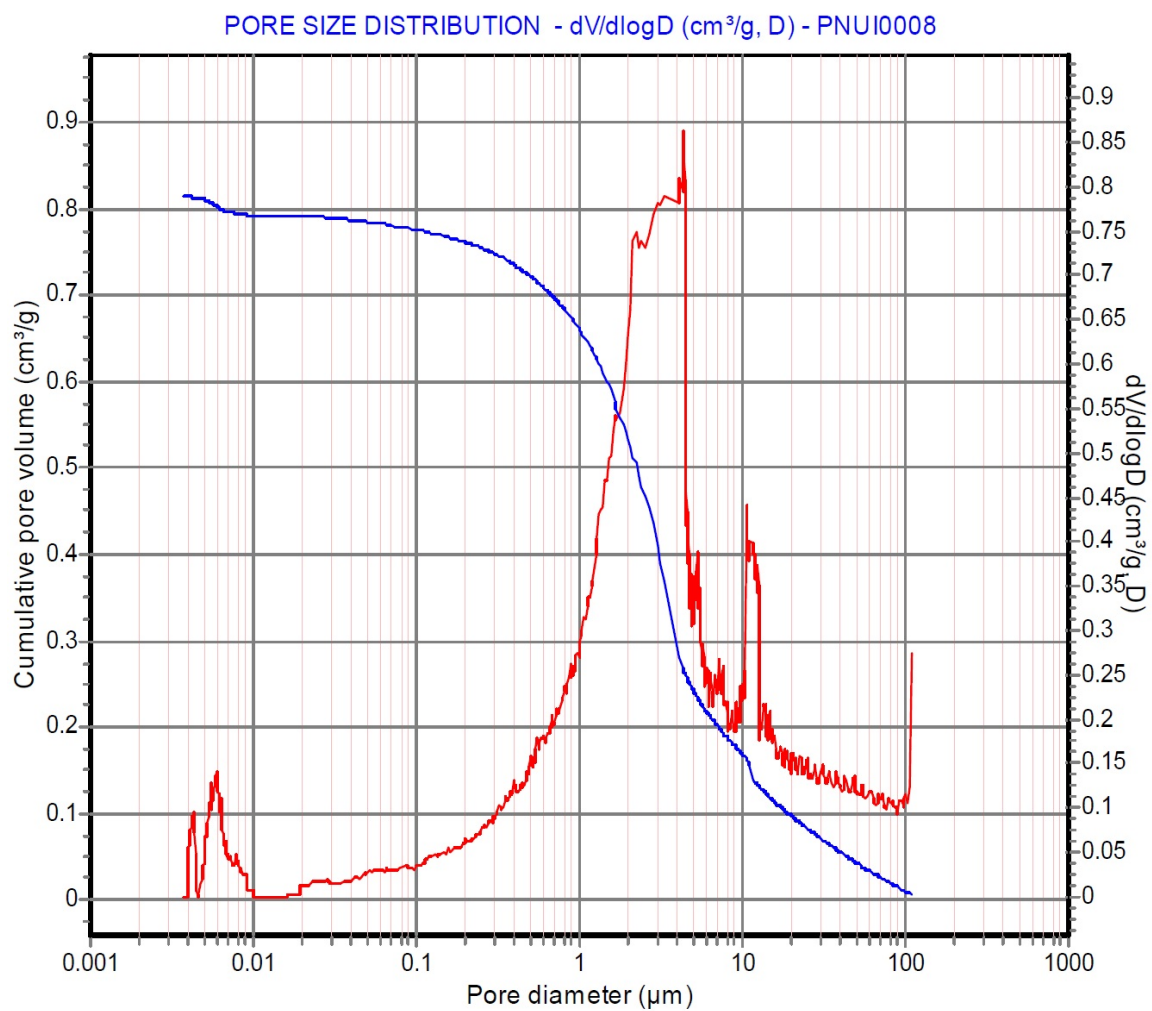


Figure S-8: Cumulative pore volume ($\text{mm}^3 \text{g}^{-1}$) and pore size distribution, $dV/d\log D$ ($\text{mm}^3 \text{g}^{-1}, D$) of anthracite.

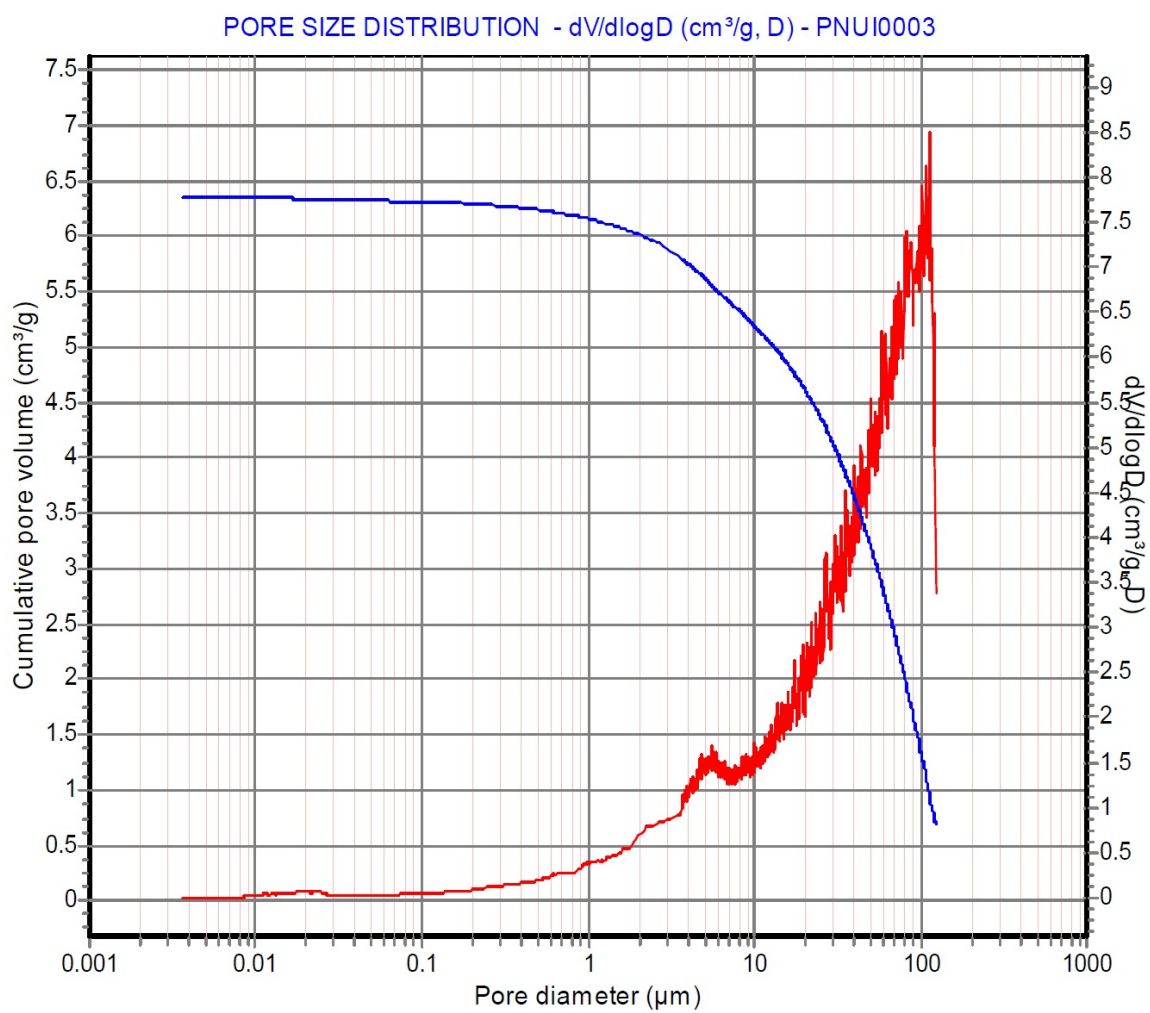


Figure S-9: Cumulative pore volume ($\text{mm}^3 \text{ g}^{-1}$) and pore size distribution, $dV/d\log D$ ($\text{mm}^3 \text{ g}^{-1}$, D) of pulverized coal briquette using starch as a binder.

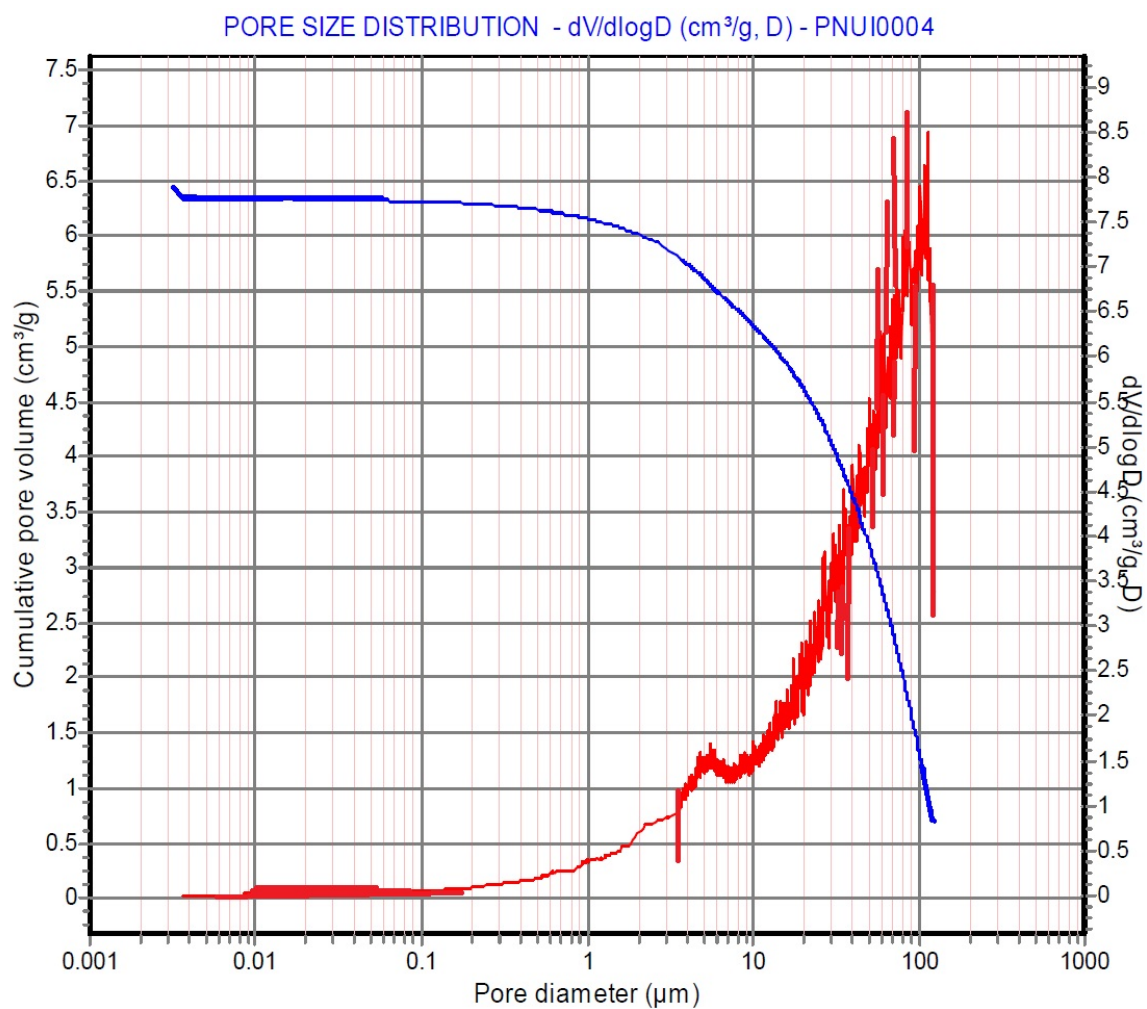


Figure S-10: Cumulative pore volume ($\text{mm}^3 \text{ g}^{-1}$) and pore size distribution, $dV/d\log D$ ($\text{mm}^3 \text{ g}^{-1}$, D) of pulverized coal briquette using resin as a binder.

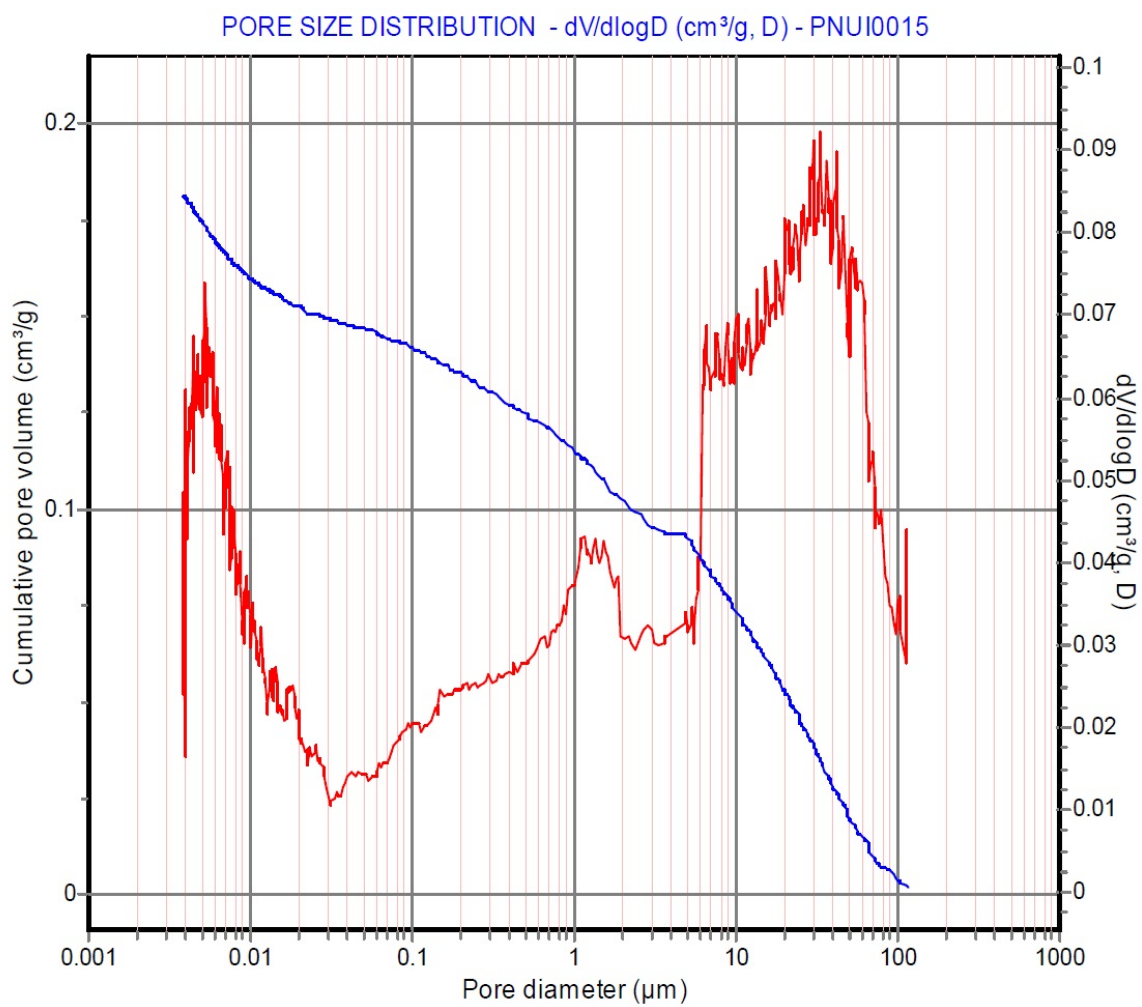


Figure S-11: Cumulative pore volume ($\text{mm}^3 \text{ g}^{-1}$) and pore size distribution, $dV/d\log D$ ($\text{mm}^3 \text{ g}^{-1}, D$) of raw olive stones.

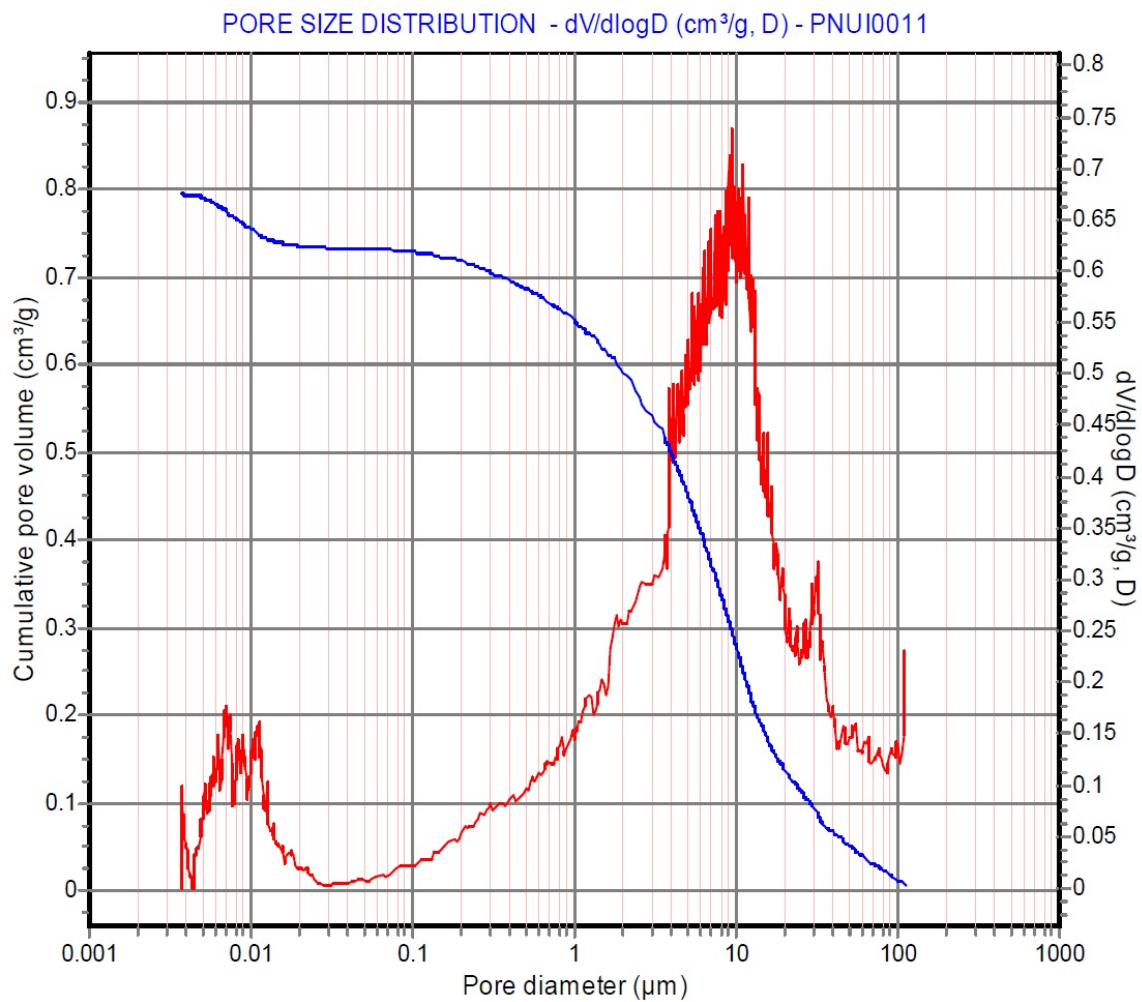


Figure S-12: Cumulative pore volume ($\text{mm}^3 \text{ g}^{-1}$) and pore size distribution, $dV/d\log D$ ($\text{mm}^3 \text{ g}^{-1}, D$) of torrefied olive stones.

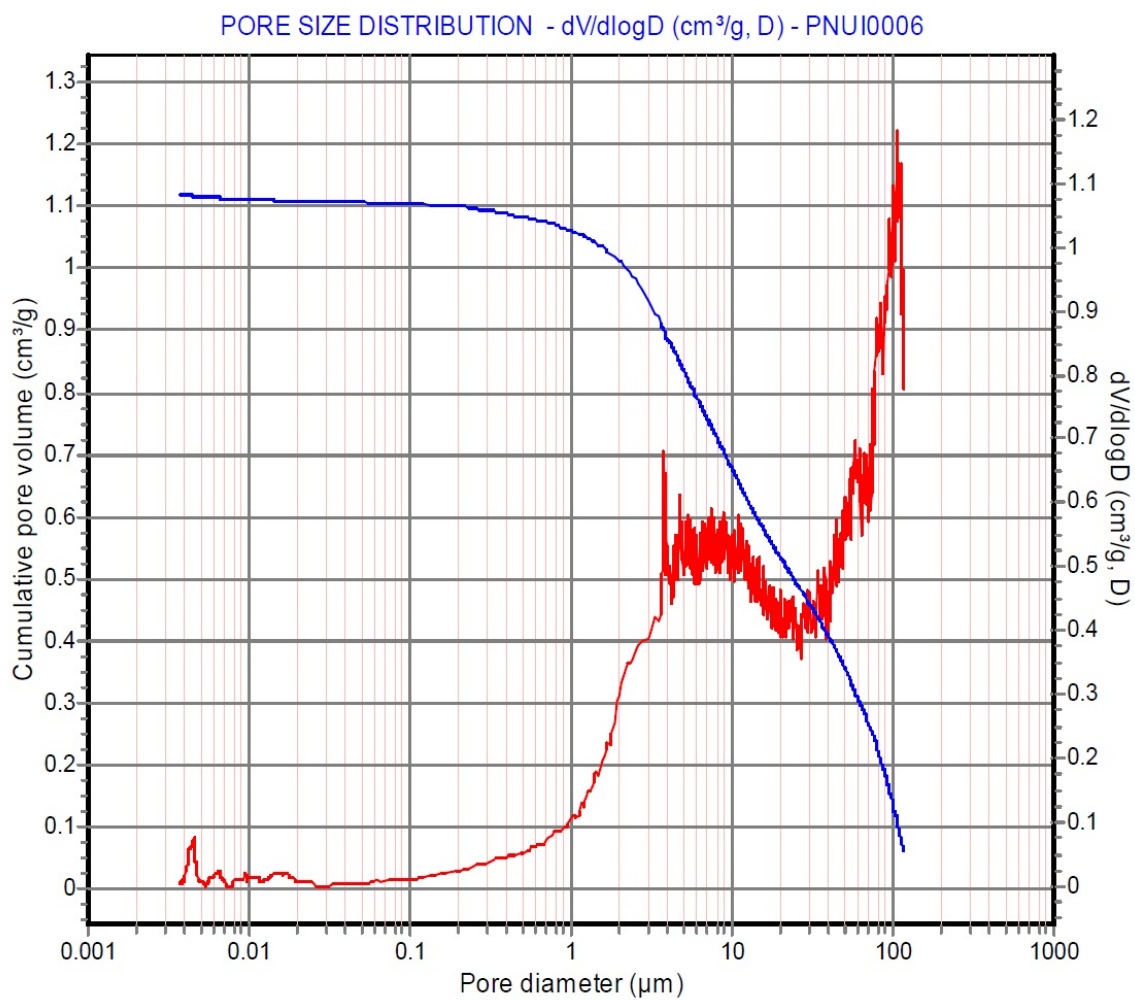


Figure S-13: Cumulative pore volume ($\text{mm}^3 \text{ g}^{-1}$) and pore size distribution, $dV/d\log D$ ($\text{mm}^3 \text{ g}^{-1}, D$) of raw woodchips.

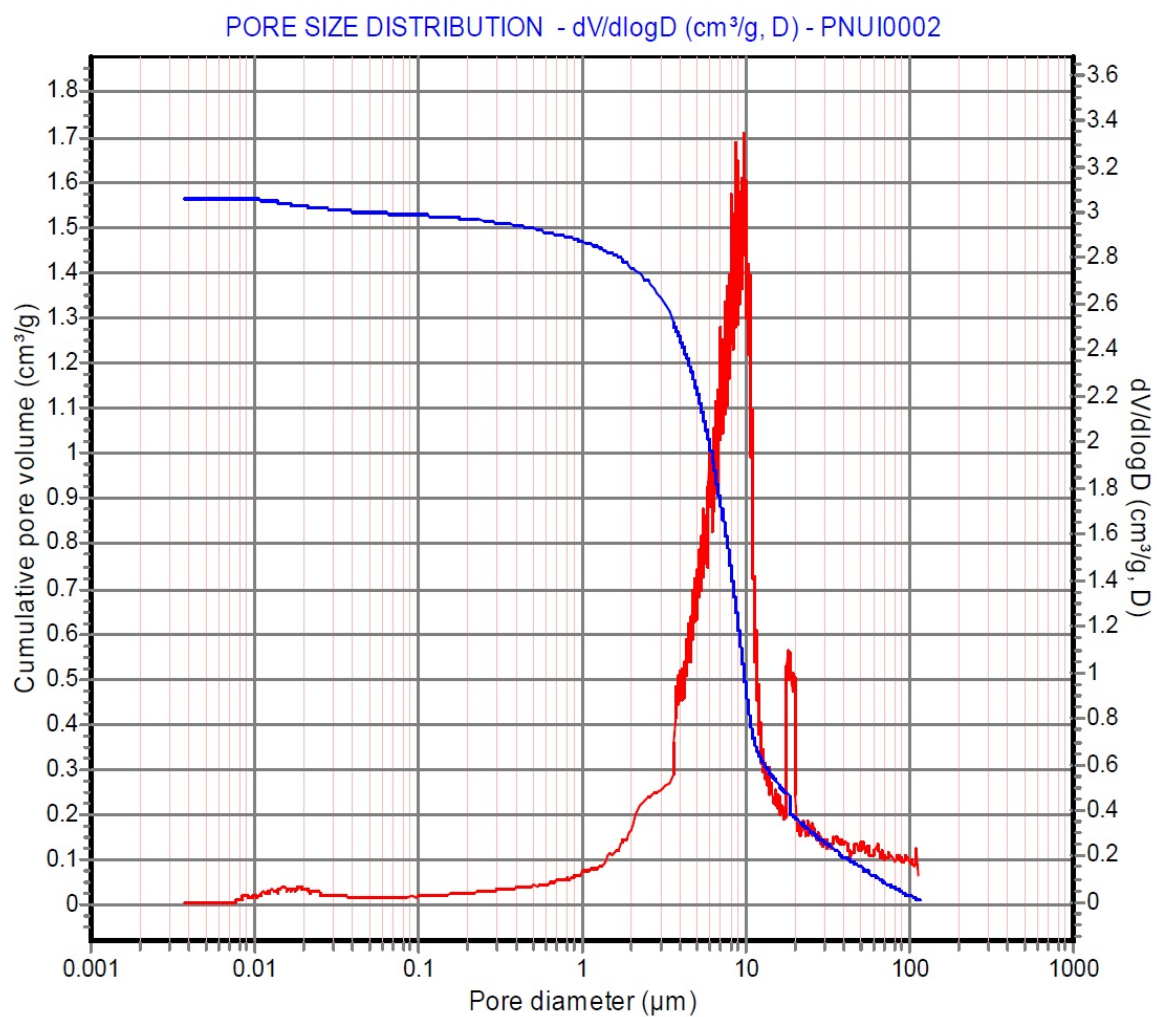


Figure S-14: Cumulative pore volume ($\text{mm}^3 \text{ g}^{-1}$) and pore size distribution, $dV/d\log D$ ($\text{mm}^3 \text{ g}^{-1}, D$) of torrefied woodchips.

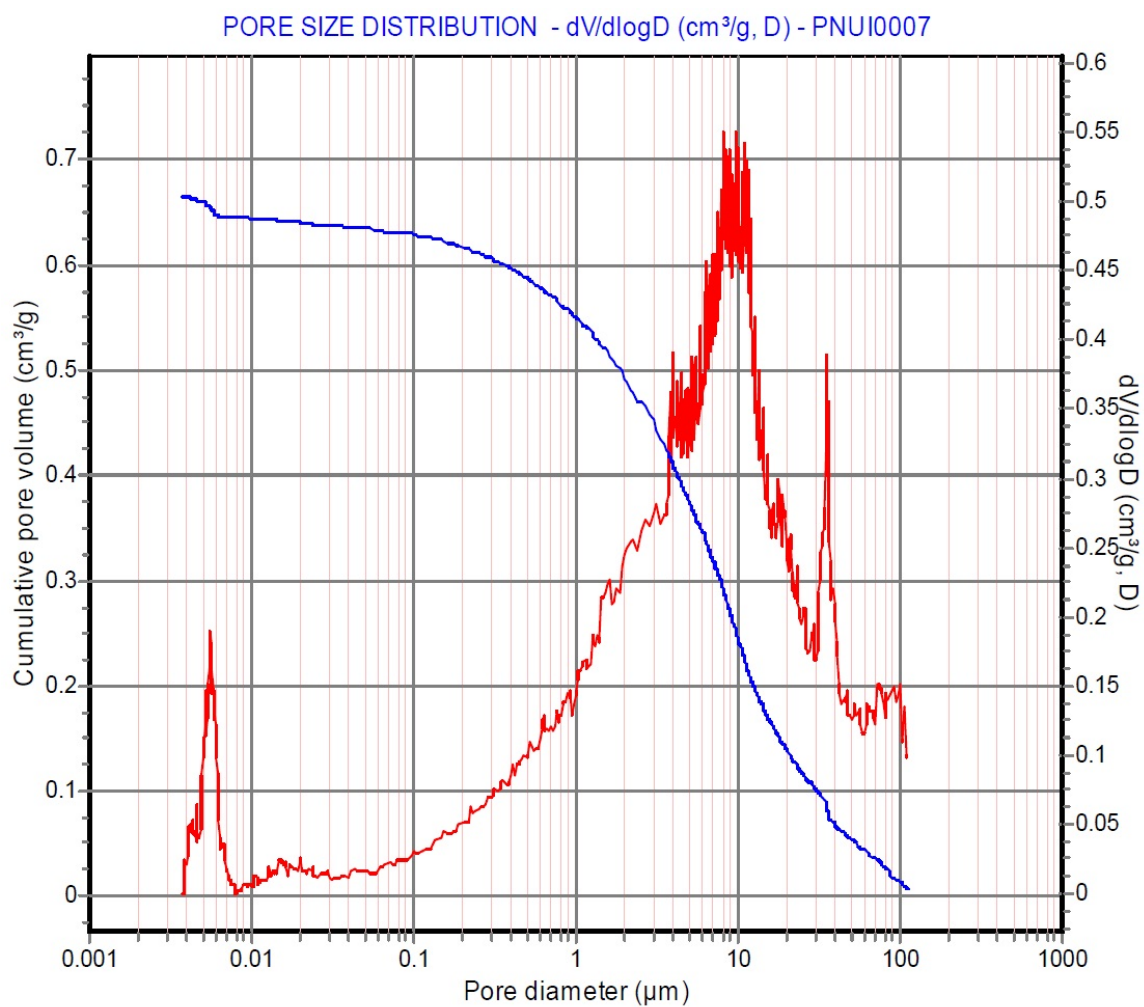
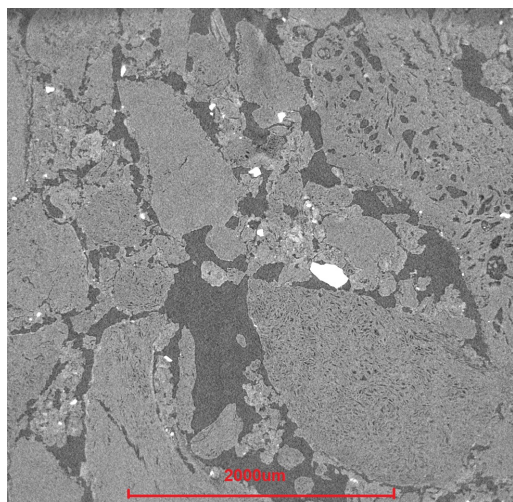
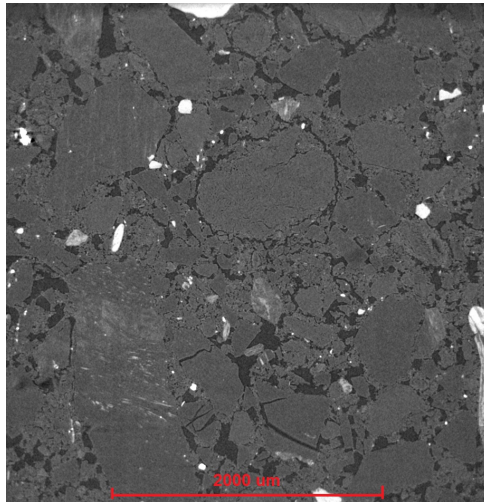


Figure S-15: Cumulative pore volume ($\text{mm}^3 \text{ g}^{-1}$) and pore size distribution, $dV/d\log D$ ($\text{mm}^3 \text{ g}^{-1}, D$) of torrefied olive stones with the higher binder content.

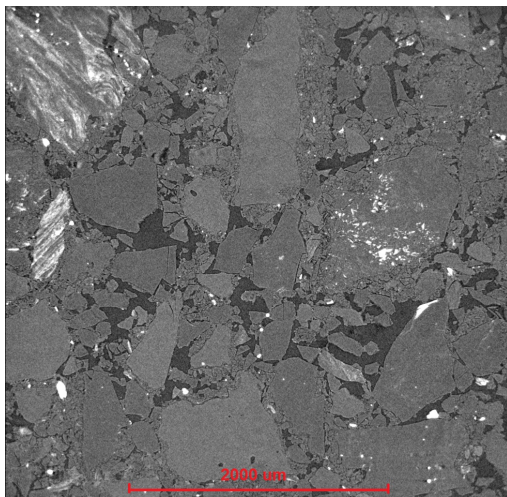
S-8. X-ray microtomography



16(a): Biomass cube



16(b): Coal cube (starch binder)



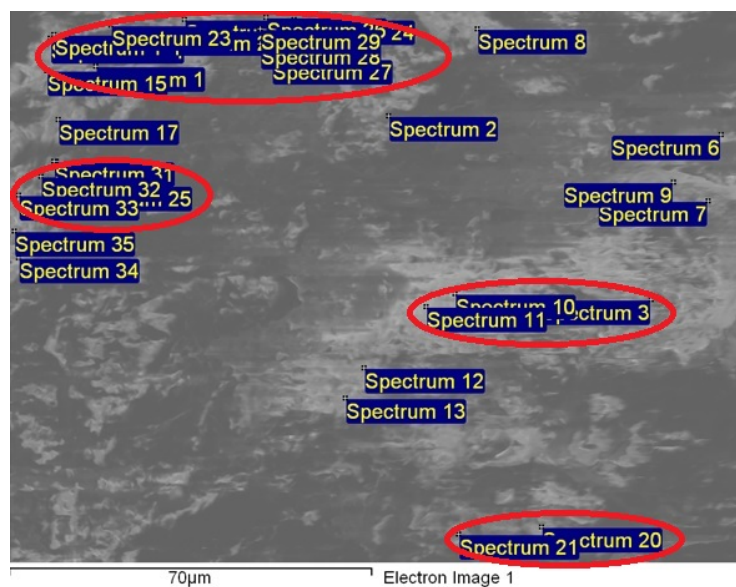
16(c): Coal cube (resin binder)

Figure S-16: X μ CT imaging analysis of biomass briquette using starch binder and coal briquettes using starch or resin binder.

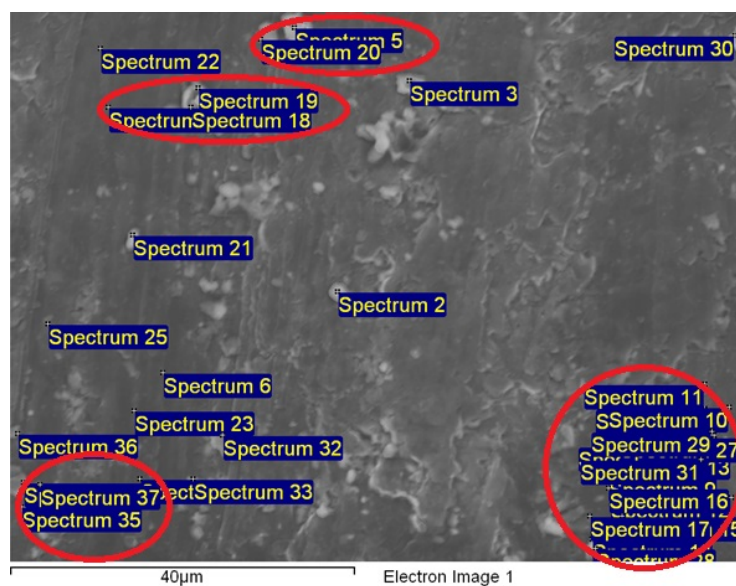
S-9. SEM-EDS analysis

Table S-2: Mean element concentrations with the standard deviation of torrefied olive stones and coal briquette from SEM-EDS analysis.

Sample		C	O	Na	Mg	Al	Si	S	Cl	K	Ca
Torrefied olive stones	Composition, %	62.9	24.4	0.8	0.07	0.62	0.3	0.46	1.57	3.9	4.95
	Std. deviation, %	11.9	6.4	0.6	0.07	0.8	0.37	0.48	3	3.9	6.3
Coal briquette	Composition, %	87.5	4.25	0.07	0.13	0.15	6.8	0.03		1.03	0.03
	Std. deviation, %	8.9	5.8	0.17	0.34	0.38	1.95	0.08		4.3	0.09



17(a): Torrefied olive stones



17(b): Coal briquette (starch)

Figure S-17: SEM-EDS analysis of torrefied olive stones and coal briquette. The red marked regions contained greater concentrations of K, Ca, Si, Al than the non-marked spectra. Mostly all spectra from torrefied olive stones contained high concentrations of Cl and S.

S-10. Solid-state NMR Spectroscopy

Table S-3: Solid-state ^{13}C NMR acquisition and processing parameters.

	number of transients	recycle delay	contact time	line broadening
		s	ms	Hz
raw woodchips	2430	3	0.5	5
torrefied woodchips	4860	2	0.5	5
high binder torrefied woodchips	4860	2	0.5	5
raw olive stones	2430	3	1	5
anthracite	4860	3	0.1	5
torrefied olive stones	4860	3	2	20
coal briquette	4860	2	0.1	5

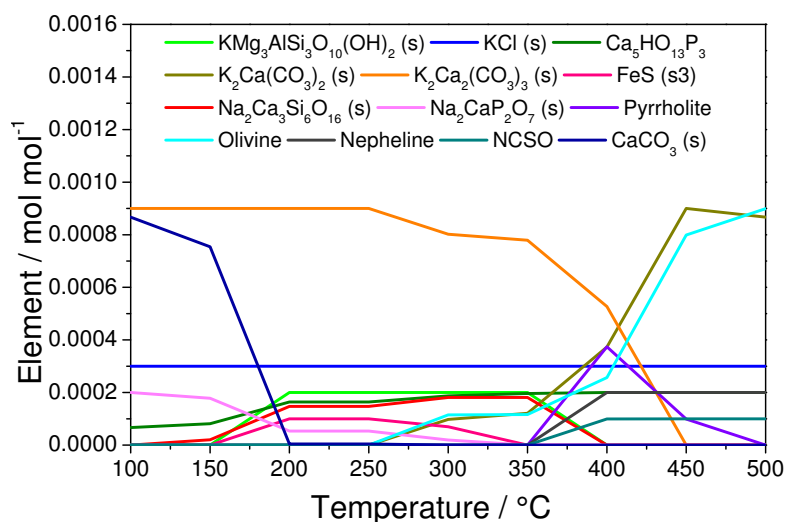
Table S-4: Resonance assignment of ^{13}C CP/MAS spectra of anthracite, coal briquettes, original woodchips and olive stones and torrefied biomass [4–8].

Chemical shift, ppm	Description
172-174	Carbohydrate; -COO-R, $\text{CH}_3\text{-COO-}$
153-154	Lignin; S3(e), S5(e)
145-148	Lignin; S3(ne), S5(ne), G1(e), G4(e)
133-138	Lignin; S1(e), S4(e), G1(e)
133-138	Lignin; S1(e), S4(e), G1(e)
126-128	highly condensated PAHs
105-106	Carbohydrates; C1, Lignin; S2, S6
89-92	C4 in cellulose (cr)
84-85	C4 in cellulose (am)
72-75	C2, C3 in carbohydrates; C5 in cellulose
63-65	CH_2OH (C6 in cellulose, C5 in xylan)
56-57	Lignin, OCH_3
30-38	CH_2 in aliphatics; mobile $\text{C}(\text{CH}_2)_n\text{C}$ in coal)
25-0	Carbohydrates; CH_3 in aliphatics

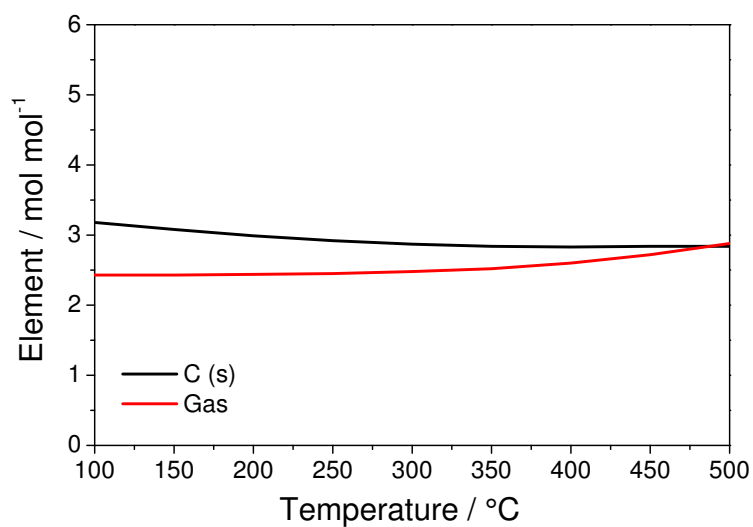
Abbreviations: S, syringyl; G, guaiacyl; ne, in non-etherified arylglycerol β -aryl ethers; e, in etherified arylglycerol β -aryl ethers.

S-11. Thermodynamic calculations with FactSage

Phase composition of the samples studied can be estimated with the help of thermodynamic calculations using the appropriate software and thermodynamic databases. Thermodynamic properties and phase equilibria of a complex system containing fuel, biomass, slag, ash, etc. for which the measurements are time-consuming and experimentally difficult (due to volatility of the components or high melting points) can be calculated and predicted in the unknown regions of temperature and composition. A thermodynamic database includes the optimized parameters (Gibbs energy) using suitable thermodynamic models for each phase. According to CALPHAD-type methodology all available experimental data (phase equilibria, mixing properties, activity, etc.) are critically analysed in terms of their consistency. Each solid or liquid phase in the system is treated by an appropriate Gibbs energy model with adjustable parameters (Gibbs energy of constituents, interaction parameters), which are optimised in accordance with the experimental information in order to generate a self-consistent dataset of Gibbs energies of all phases in a system.

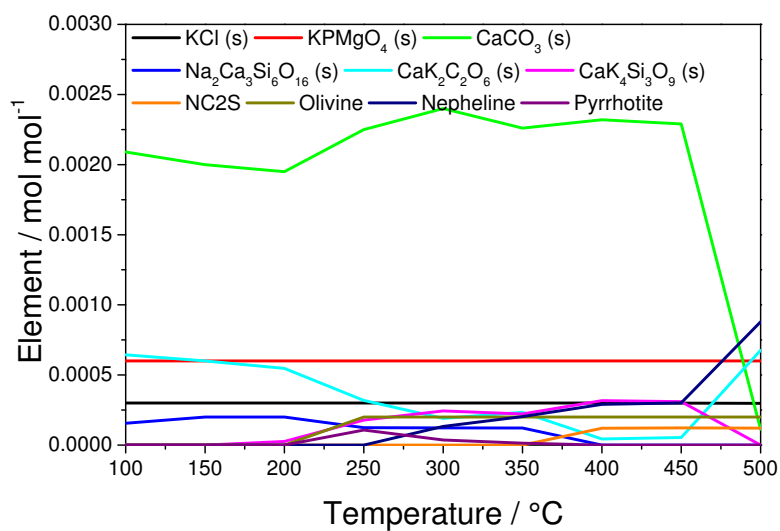


18(a): Inorganic compounds

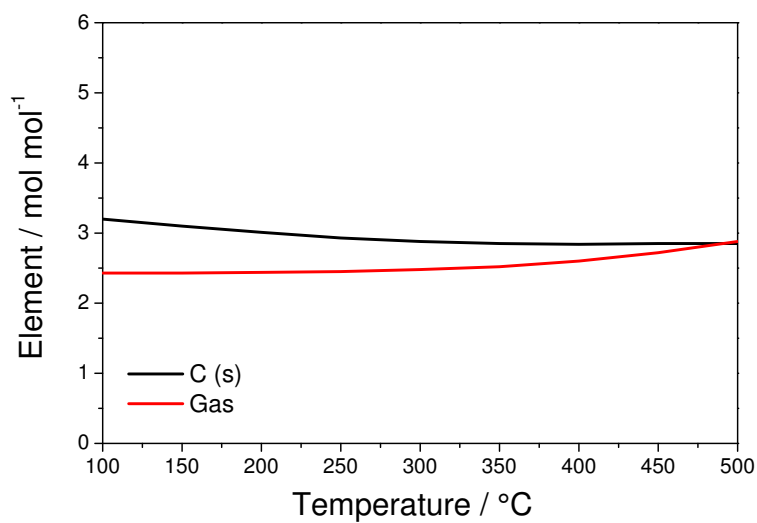


18(b): Solid carbon and gas

Figure S-18: Output results of FactSage calculation using FToxid database with the main inorganic components of raw woodchips: (a) inorganic stoichiometric compounds and solid solutions and (b) solid carbon and gas.

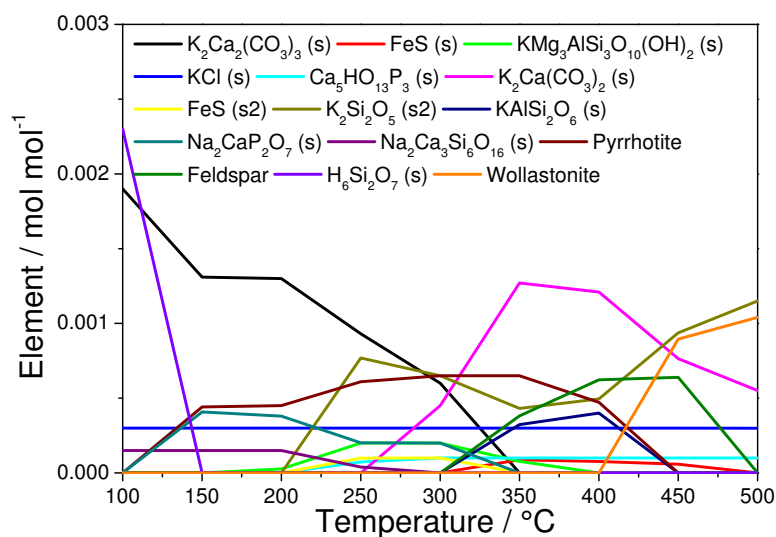


19(a): Inorganic compounds

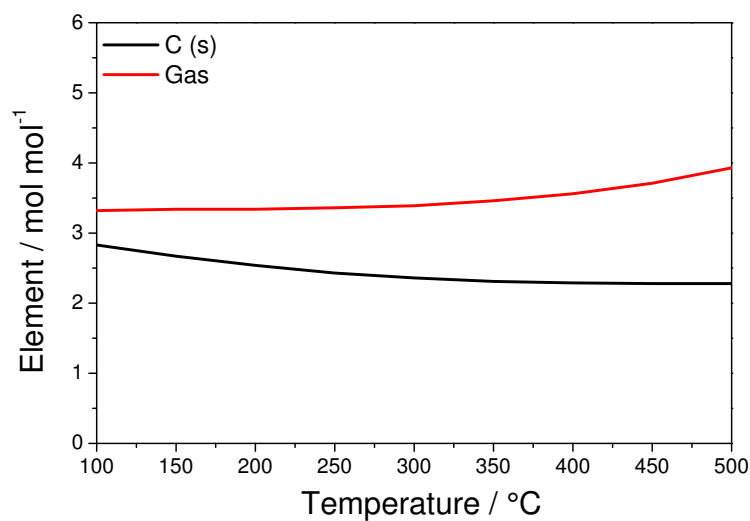


19(b): Solid carbon and gas

Figure S-19: Output results of FactSage calculation using GTOX database with the main inorganic components of raw woodchips: (a) inorganic stoichiometric compounds and solid solutions and (b) solid carbon and gas.

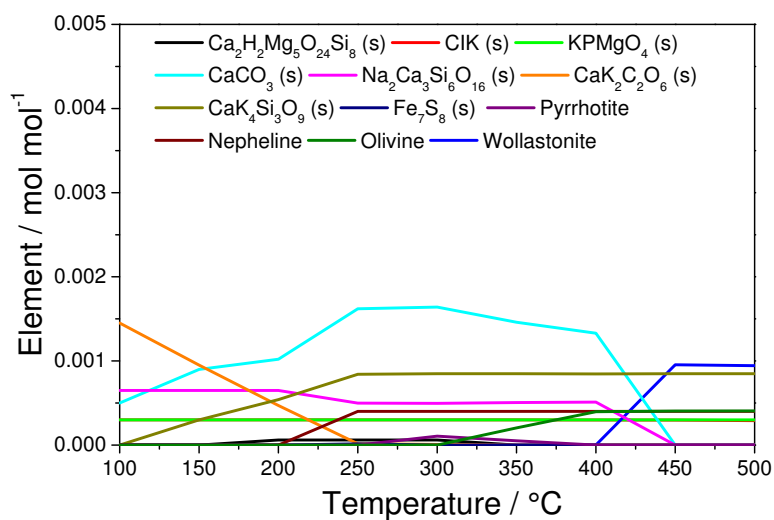


20(a): Inorganic compounds

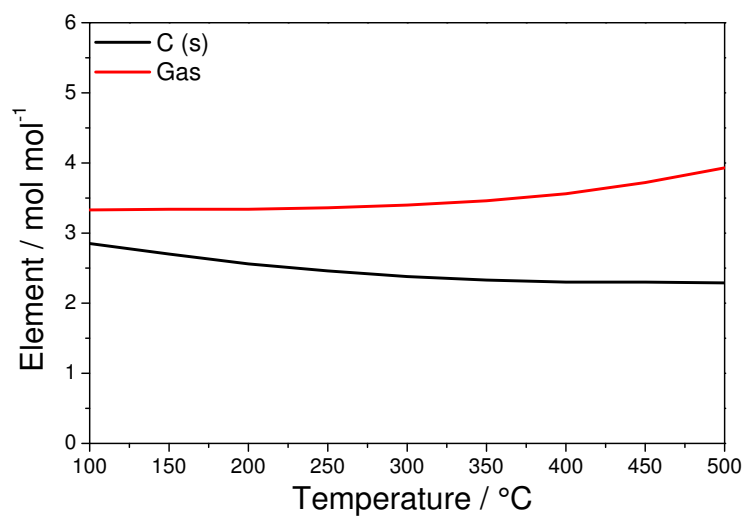


20(b): Solid carbon and gas

Figure S-20: Output results of FactSage calculation using FToxid database with the main inorganic components of raw olive stones: (a) inorganic stoichiometric compounds and solid solutions and (b) solid carbon and gas.

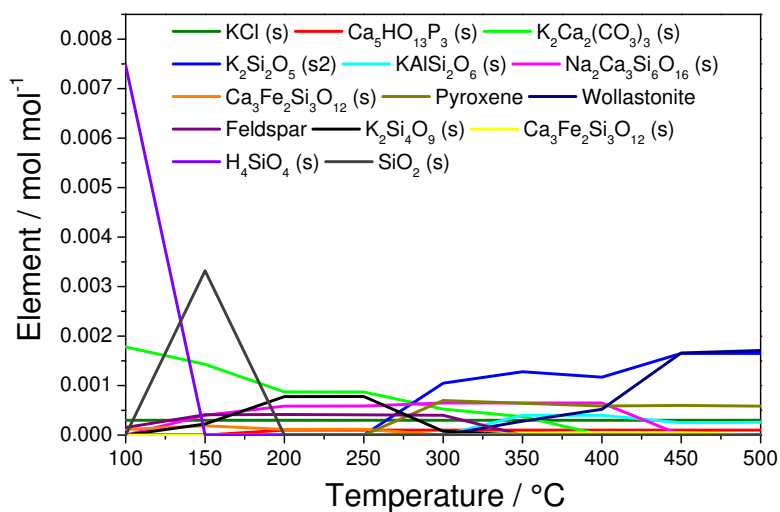


21(a): Inorganic compounds

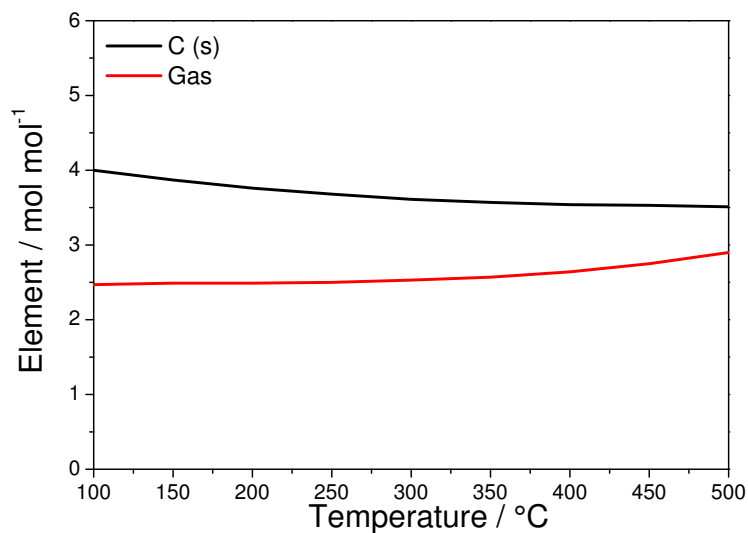


21(b): Solid carbon and gas

Figure S-21: Output results of FactSage calculation using GTOX database with the main inorganic components of raw olive stones: (a) inorganic stoichiometric compounds and solid solutions and (b) solid carbon and gas.

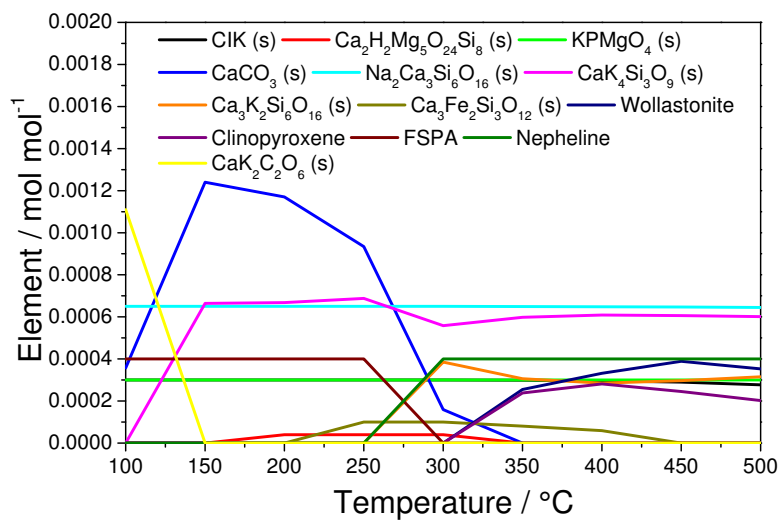


22(a): Inorganic compounds

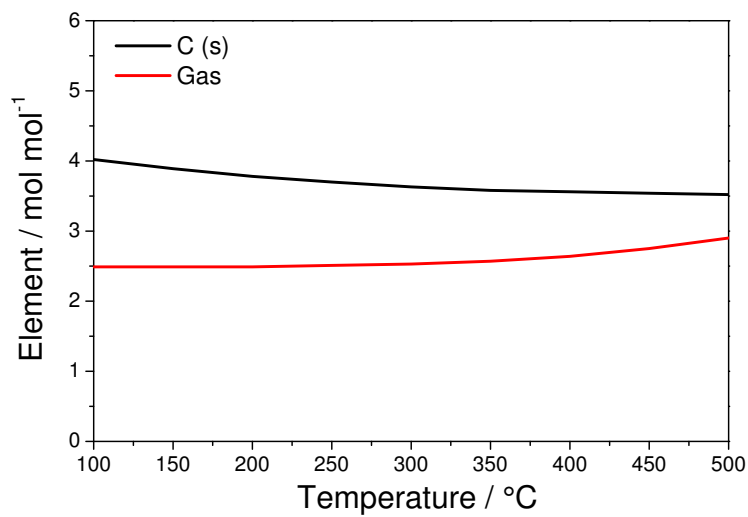


22(b): Solid carbon and gas

Figure S-22: Output results of FactSage calculation using FToxid database with the main inorganic components of torrefied woodchips: (a) inorganic stoichiometric compounds and solid solutions and (b) solid carbon and gas.

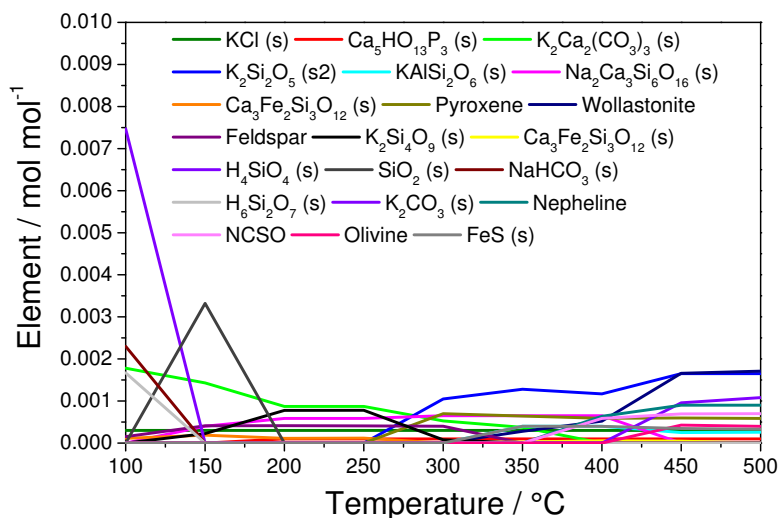


23(a): Inorganic compounds

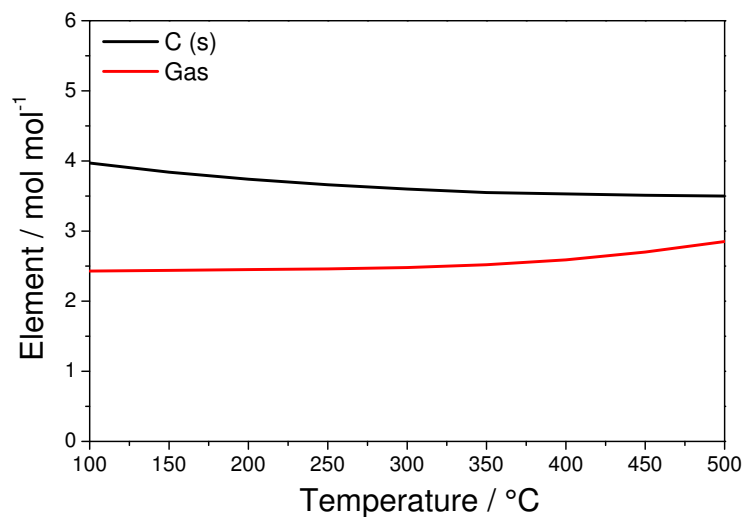


23(b): Solid carbon and gas

Figure S-23: Output results of FactSage calculation using GTOX database with the main inorganic components of torrefied woodchips: (a) inorganic stoichiometric compounds and solid solutions and (b) solid carbon and gas.

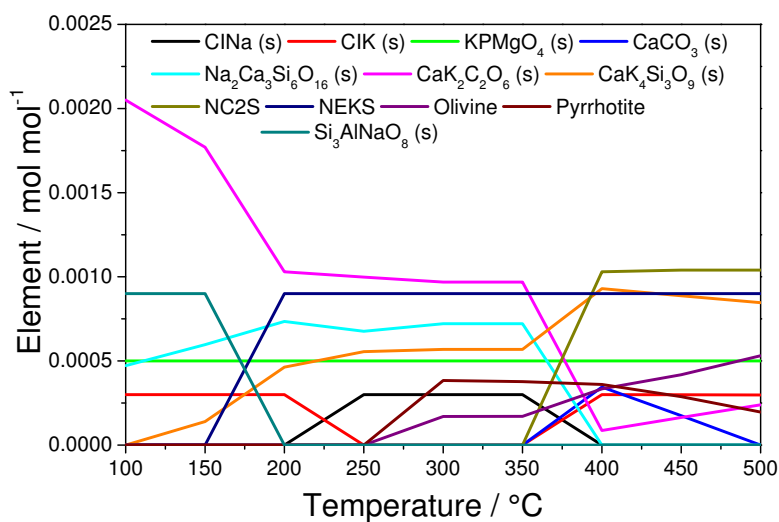


24(a): Inorganic compounds

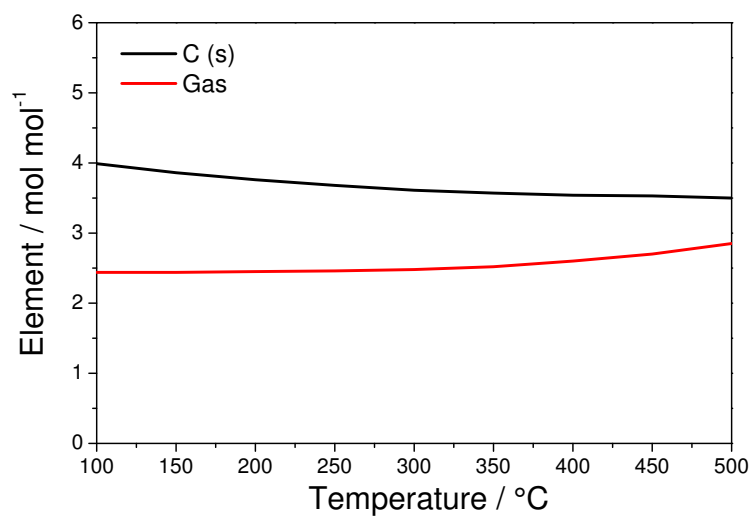


24(b): Solid carbon and gas

Figure S-24: Output results of FactSage calculation using FToxid database with the main inorganic components of torrefied olive stones: (a) inorganic stoichiometric compounds and solid solutions and (b) solid carbon and gas.

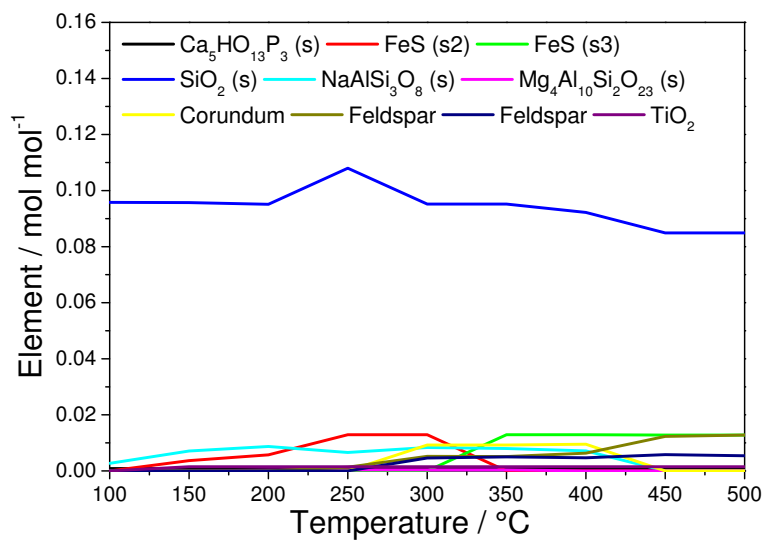


25(a): Inorganic compounds

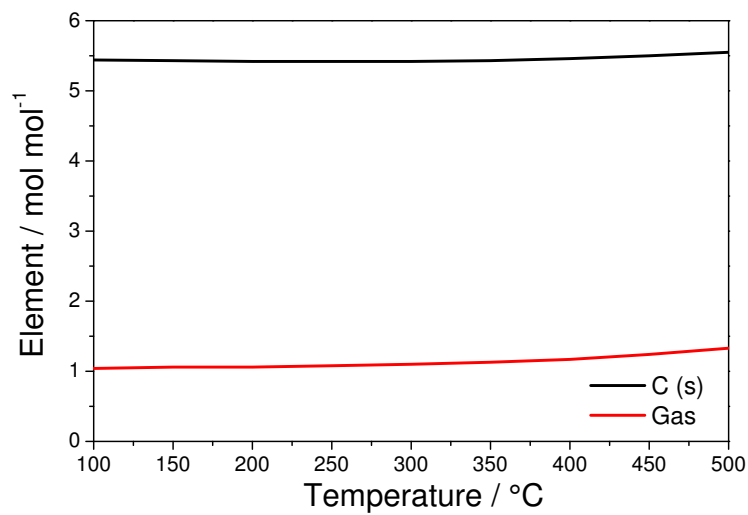


25(b): Solid carbon and gas

Figure S-25: Output results of FactSage calculation using GTOX database with the main inorganic components of torrefied olive stones: (a) inorganic stoichiometric compounds and solid solutions and (b) solid carbon and gas.

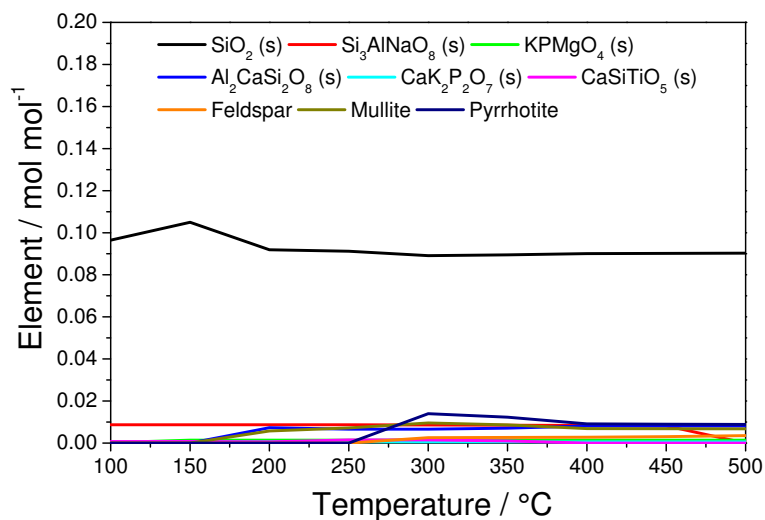


26(a): Inorganic compounds

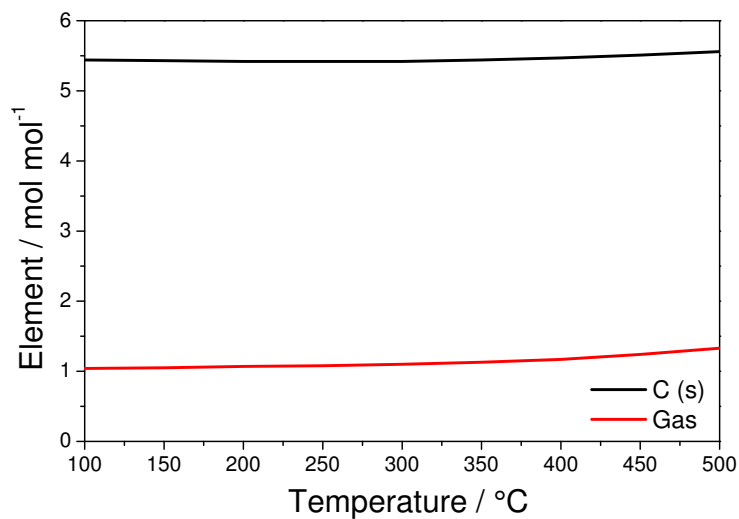


26(b): Solid carbon and gas

Figure S-26: Output results of FactSage calculation using FToxid database with the main inorganic components of anthracite: (a) inorganic stoichiometric compounds and solid solutions and (b) solid carbon and gas.



27(a): Inorganic compounds



27(b): Solid carbon and gas

Figure S-27: Output results of FactSage calculation using GTOX database with the main inorganic components of anthracite: (a) inorganic stoichiometric compounds and solid solutions and (b) solid carbon and gas.

S-12. Elemental analysis

Figure S-28 shows a Van Krevelen plot of raw olive stones and woodchips, torrefied material, torrefied woodchips with the high starch content, anthracite, pulverized coal briquette using starch or resin as a binder. Results contained in Figure S-28 indicate that oxygen and hydrogen content in torrefied samples decreases. Elemental compositions of pulverized coal briquettes using starch or resin were comparable to the composition of anthracite, indicating no influence of a binder on the elemental composition of coal briquettes.

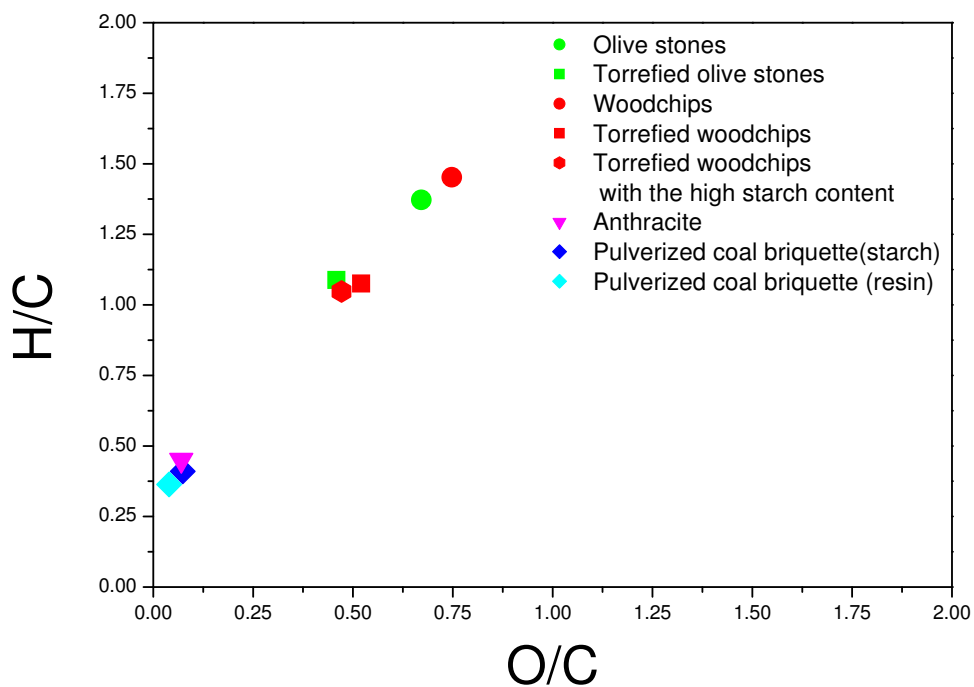


Figure S-28: Van Krevelen plot of raw olive stones and woodchips, torrefied material, torrefied woodchips with the high starch content, anthracite, pulverized coal briquette using starch or resin as a binder.

S-13. X-ray diffraction

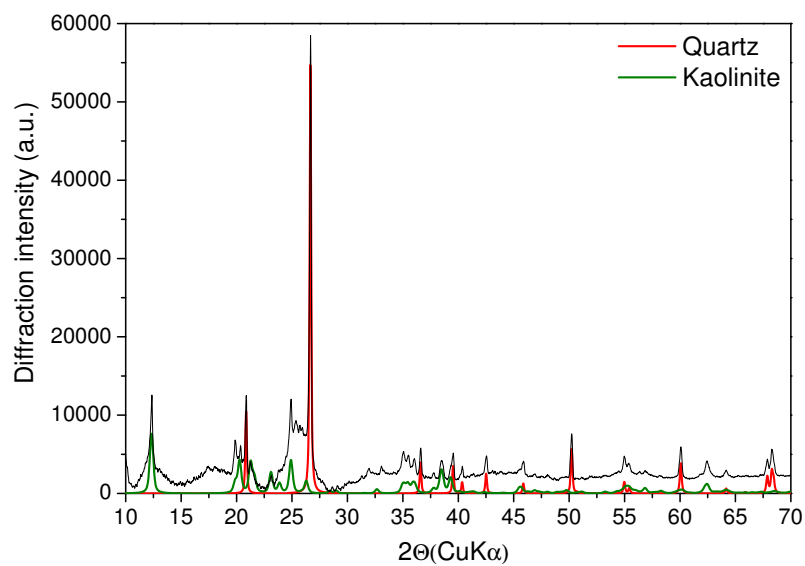


Figure S-29: XRD measurements of anthracite. The XRD patterns were assigned to kaolinite and quartz.

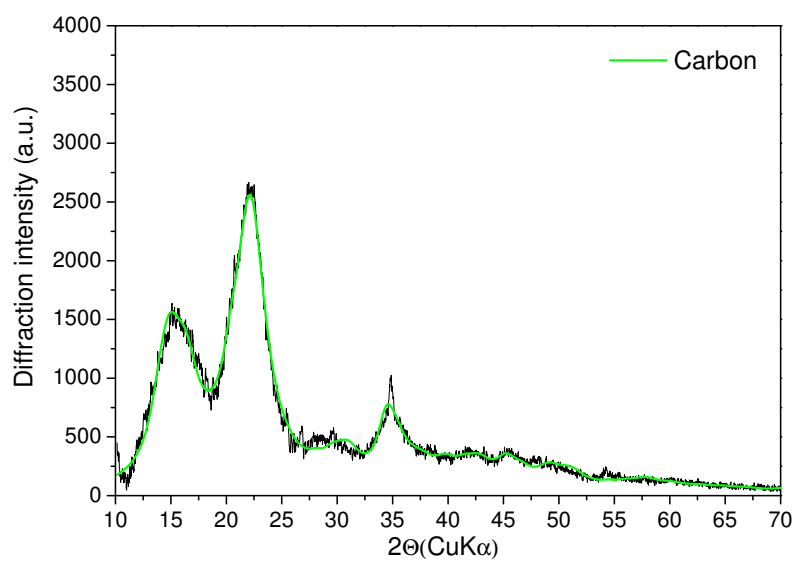
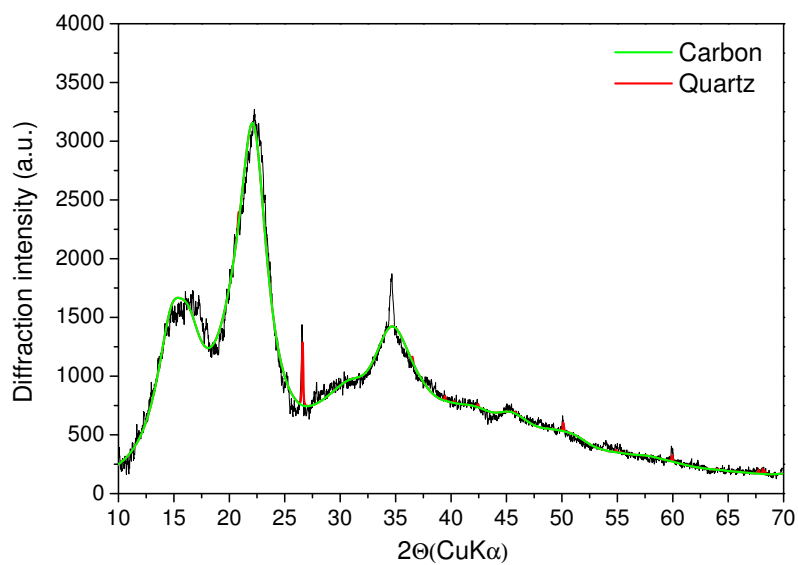
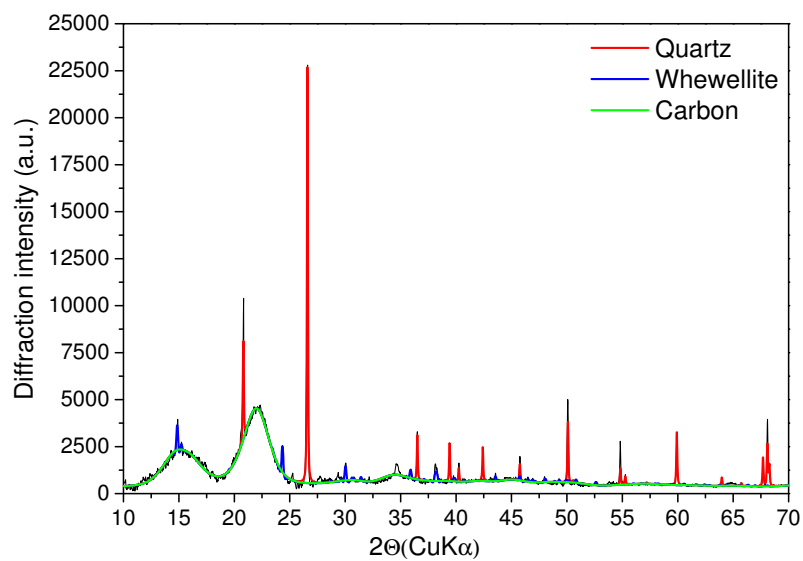
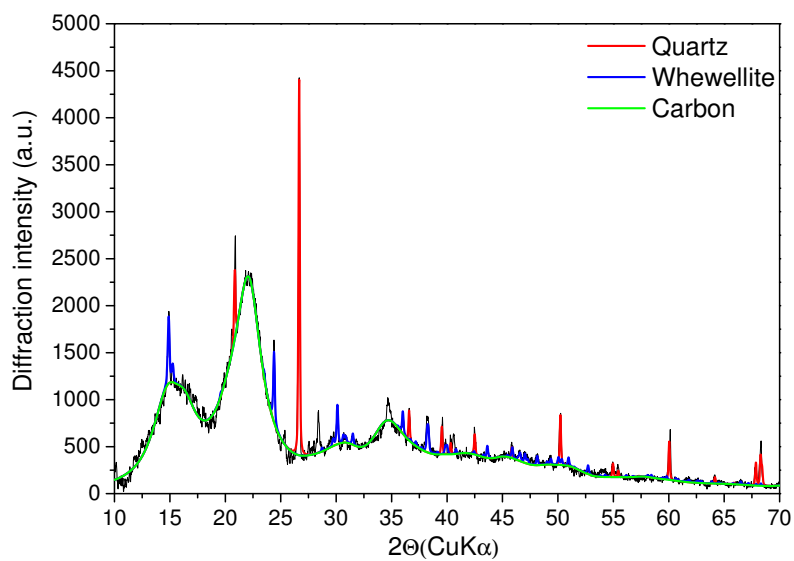


Figure S-30: XRD measurements of original woodchips and torrefied biomass. The XRD patterns were assigned to carbon and quartz.



31(a): Olive stones



31(b): Torrefied olive stones

Figure S-31: XRD measurements of original olive stones and torrefied biomass. The XRD patterns were assigned to carbon, quartz, and whewellite.

References

- [1] Saad ES, Mostafa ME, Analysis of Grain Size Statistic and Particle Size Distribution, Waste Biomass Valor 5 (2014) 1005–18.
- [2] Williams O, Newbolt G, Eastwick C, Kingman S, Giddings D, Lester E et al., Influence of mill type on densified biomass comminution, Applied Energy 182 (2016) 219–31.
- [3] Gavlighi HA, Meyer AS, Zaidel DNA, Mohammadifar MA, Mikkelsen JD, Stabilization of emulsions by gum tragacanth (*Astragalus* spp.) correlates to the galacturonic acid content and methoxylation degree of the gum, Food Hydro 31 (2013) 5–14.
- [4] Xu F, Sun JX, Sun RC, Fowler P, Baird M, Comparative study of organo-solv lignins from wheat straw, Ind Crops Products 23 (2) (2006) 180–93.
- [5] Webster EA, Chudek JA, Hopkins DW, Carbon transformations during decomposition of different components of plant leaves in soil, Soil Biol Biochem 32 (3) (2000) 301–14.
- [6] Reid DG, Bonnet SL, Kemp G, van der Westhuizen JH, Analysis of commercial proanthocyanidins. Part 4: Solid state ^{13}C NMR as a tool for in situ analysis of proanthocyanidin tannins, in heartwood and bark of quebracho and acacia, and related species, Photochem 94 (2013) 243–8.
- [7] Hicham L, Ismaili-Alaoui M, Gaime I, Roussos S, Abstract for Characterization of dried mixture of olive cake with olive mill wastewater: elemental, spectroscopic analyses FTIR and ^{13}C -NMR, Olivebioteq conference, 15th September 2009, pages 657-63 .

- [8] Baccile N, Falco C, Titirici MM, Characterization of biomass and its derived char using ^{13}C -solid state nuclear magnetic resonance, *Green Chem* 16 (2014) 4839–69.